

# Joint Design for RIS-Aided ISAC via Deep Unfolding Learning

Jifa Zhang<sup>1b</sup>, Mingqian Liu<sup>1b</sup>, *Member, IEEE*, Jie Tang<sup>2b</sup>, *Senior Member, IEEE*,  
Nan Zhao<sup>1b</sup>, *Senior Member, IEEE*, Dusit Niyato<sup>3b</sup>, *Fellow, IEEE*, and Xianbin Wang<sup>4b</sup>, *Fellow, IEEE*

**Abstract**—Integrated sensing and communication (ISAC) has become a promising technique to alleviate the spectrum congestion via sharing the same spectrum for communication and sensing. Nevertheless, many ISAC schemes encounter the challenges of high computational complexity. Thanks to the powerful non-linear fitting capabilities and fast inference speed, deep learning is expected to facilitate the online deployment of ISAC. In this paper, we propose a dual-functional waveform design scheme for reconfigurable intelligent surface (RIS) aided ISAC based on deep unfolding learning. Specifically, the weighted sum of multi-user interference energy and waveform discrepancy is minimized via the joint waveform and phase-shift design. We first develop an alternating direction method of multipliers (ADMM) based iterative algorithm to handle the non-convex optimization problem. Then, we develop a deep unfolding neural network (NN), named ADMM-NET, which unfolds the proposed ADMM-based iterative algorithm to a layer-wise architecture and replaces the matrix inversions with low-complexity approximations. In addition, we present a black-box NN for performance comparison. Simulation results verify that the ADMM-NET outperforms the black-box NN in performance, interpretability and training samples. Moreover, the ADMM-NET is superior to the ADMM-based iterative algorithm in both computational complexity and performance, facilitating the online deployment.

**Index Terms**—ADMM, deep unfolding, ISAC, RIS, waveform design.

## I. INTRODUCTION

NOWADAYS, the exponential growth of wireless data traffic has significantly exacerbated the spectrum congestion, which requires urgent solutions. Recently, integrated sensing and communication (ISAC) is emerging as a promising technique to achieve dual services while boosting the spectrum efficiency [2], [3]. In particular, the communication and sensing are integrated into a single unified platform, sharing the same spectrum and hardware [4]. Therefore, ISAC outperforms the separate setups in energy consumption, hardware size, spectrum efficiency and interference mitigation, enabling its various applications in wireless communications, such as vehicle-to-everything (V2X) [5], [6], Internet of Things (IoT) [7], [8], and smart home [9]. As a popular area, ISAC has attracted enormous research interests.

Recently, great efforts have been devoted to facilitating the ISAC from diverse perspectives, such as signal processing, software protocol and hardware architecture [10]. Waveform design, as an essential part of ISAC, aims at obtaining the dual-functional (DF) waveform for both communication and sensing. In general, DF waveform design schemes can be categorized into the radar-centric, communication-centric, and joint-design ones. Radar-centric schemes embed the communication symbols into the typical radar waveforms via various signalling strategies, such as amplitude modulation [11], phase modulation [12], and index modulation [13]. Although satisfactory sensing performance can be guaranteed, the achievable rate of radar-centric schemes may not meet the communication requirement owing to the inherent limitation of radar waveforms. In contrast, the communication-centric schemes usually leverage the high-flexibility communication waveforms, such as orthogonal frequency-division multiplexing (OFDM), for additional sensing functionality, which can achieve high achievable rate [14]. Owing to the randomness nature, communication waveforms encounter the drawbacks of high peak-to-average-power ratio, non-constant modulus and poor auto-correlation property, resulting in the degradation of sensing capability. Different from the above-mentioned schemes, the joint-design ones directly optimize the DF waveform according to the communication and sensing requirements, which can keep a better balance between two functionalities [15]. For example,

Manuscript received 19 May 2024; revised 5 August 2024; accepted 12 August 2024. Date of publication 19 August 2024; date of current version 7 February 2025. The work of Nan Zhao is supported in part by the National Natural Science Foundation of China (NSFC) under Grant U23A20271. The work of Dusit Niyato is supported by the National Research Foundation, Singapore, and Infocomm Media Development Authority under its Future Communications Research & Development Programme, Defence Science Organisation (DSO) National Laboratories under the AI Singapore Programme (AISG Award No: AISG2-RP-2020-019 and FCP-ASTAR-TG-2022-003), Singapore Ministry of Education (MOE) Tier 1 (RG87/22), and the NTU Centre for Computational Technologies in Finance (NTU-CCTF). Part of this paper is submitted to IEEE WCSP 2024 [1]. The associate editor coordinating the review of this article and approving it for publication was G. Han. (*Corresponding author: Nan Zhao.*)

Jifa Zhang and Nan Zhao are with the School of Information and Communication Engineering, Dalian University of Technology, Dalian 116024, Liaoning, China (e-mail: jifazhang@mail.dlut.edu.cn; zhaonan@dlut.edu.cn).

Mingqian Liu is with the State Key Laboratory of Integrated Service Networks, Xidian University, Xi'an 710071, Shaanxi, China (e-mail: mqliu@mail.xidian.edu.cn).

Jie Tang is with the School of Electronic and Information Engineering, South China University of Technology, Guangzhou 510640, China (e-mail: eejtang@scut.edu.cn).

Dusit Niyato is with the College of Computing and Data Science, Nanyang Technological University, Singapore 639798 (e-mail: dniyato@ntu.edu.sg).

Xianbin Wang is with the Department of Electrical and Computer Engineering, Western University, London, ON N6A 5B9, Canada (e-mail: xianbin.wang@uwo.ca).

Digital Object Identifier 10.1109/TCCN.2024.3445380

Zhu et al. in [16] proposed a DF waveform to maximize the target detection probability in cluttering environment while satisfying the users' quality of service (QoS) requirements. Moreover, Liu et al. in [17] developed a symbol-level precoding-based waveform design, where the beam pattern mismatch was minimized subject to the QoS constraint of each user. In [18], Shi et al. developed a DF constant modulus waveform for reconfigurable intelligent surface (RIS)-aided ISAC system, where the transmit waveform and phase shifts of RIS were jointly optimized to minimize the weighted mean square cross-correlation pattern. Zhong et al. in [19] leveraged an RIS to assist the ISAC, and minimized the weighted sum of radar signal-to-interference-plus-noise ratio (SINR) and multi-user interference (MUI) energy via joint waveform and phase-shift design. Du et al. in [20] investigated the trade-off between communication and sensing from the perspective of DF waveform design. Therefore, the joint-design schemes are not limited by the radar or communication standards, enjoying the advantages of higher design flexibility. Nevertheless, the joint-design schemes usually involve the complicated non-convex optimization, encountering the drawback of high computational complexity.

On the other hand, deep learning (DL) has achieved significant success across diverse fields, such as content generation and machine translation, showcasing the powerful non-linear fitting and automatic feature extraction capabilities [21], [22]. Moreover, the low-complexity inference process enables the online deployment of DL [23], [24]. Motivated by these, DL is expected to handle complex optimization problems in a data-driven manner, bypassing the complicated mathematical derivation and facilitating the online implementation [25]. Since solving optimization problem is essentially to find the mapping relationship between the problem instance and the corresponding solution, it is expected that deep neural networks (DNNs) can model the complicated mappings thanks to the powerful fitting capability [26]. For example, Zhao et al. in [27] utilized a neural network (NN) to learn the mapping between the pilot and transmit beamforming, bypassing the channel estimation and achieving better communication performance than the baseline. Moreover, Liu et al. in [28] trained an NN in an unsupervised learning manner for power allocation and beamforming. In [29], a graph attention network was trained by Li et al. in a supervised learning manner to fit the mapping from channel state information to beamforming vector. However, these NNs can be regarded as black-boxes without sufficient interpretability, and require enormous training samples to tune. This poses huge challenges in their wide applications in wireless communications, especially for the scenarios with limited training samples.

To overcome these limitations, domain knowledge is expected to guide the design of NNs, motivating the research on model-driven NNs [30]. As a typical representative, deep unfolding NN unfolds the iterative algorithms to a layer-wise architecture, and each layer can be viewed as one iteration [31]. Therefore, its forward propagation is equivalent to conducting the finite iterations of underlying iterative algorithm, enhancing the interpretability significantly. Moreover, compared with the black-box counterpart, deep

unfolding NN exhibits the advantages of reduced data requirement, much less network parameters and faster convergence, receiving plenty of research interests [32]. For instance, Hu et al. in [33] developed a deep unfolding framework for sum-rate maximization, and designed an NN to solve this problem via unfolding the weighted minimum mean-square error (WMMSE) iterative algorithm, illustrating low computational complexity and satisfactory performance. In [34], an alternating direction method of multipliers (ADMM)-based deep unfolding NN was proposed by Tiba et al. for signal detection, and the penalty coefficient was learned via NN rather than being manually set. In [35], Nguyen et al. developed a deep unfolding NN based on the projected gradient descent (PGD) algorithm for hybrid beamforming design. In [36], Nguyen et al. proposed another PGD-based deep unfolding NN to optimize the ISAC hybrid beamforming. Krishnananthalingam et al. in [37] tackled the constant DF waveform design via a PGD-based deep unfolding NN, obtaining the near-optimal solution. In [38], He et al. developed a PGD-based deep unfolding framework to deal with a series of constrained optimization problems. Xu et al. in [39] proposed a deep unfolding NN for fast beamforming, leveraging its advantages of low complexity.

To the best of our knowledge, the deep unfolding NN for DF waveform design has not been well investigated, which motivates this work. Compared with the conference version [1], this paper presents more detailed description of the proposed algorithms, and a comprehensive comparison between the proposed model-driven NN and the black-box counterpart. In addition, more simulation results are provided to verify the effectiveness of the proposed algorithms. The comparison between this work and the related ones are presented in Table I, and the contributions are summarized as follows.

- This paper develops the DF waveform design for RIS-aided ISAC. To study the performance trade-off, the weighted sum of MUI energy and waveform discrepancy (WSMEWD) is minimized via jointly optimizing the transmit waveform and phase shifts of RIS. We propose an ADMM-based iterative algorithm and a low-complexity deep unfolding NN to deal with the non-convex problem, respectively.
- We first propose an ADMM-based iterative algorithm to deal with the optimization problem under consideration. In particular, the original problem is first divided into four subproblems, whose closed-form solutions are derived. Then, each subproblem is alternatively optimized until convergence.
- To further reduce the computational complexity, we develop a deep unfolding NN, which unfolds the proposed ADMM-based iterative algorithm to a layer-wise architecture and introduces the learnable parameters to approximate the high-complexity matrix inversion. Moreover, we present the comprehensive comparison between the proposed ADMM-NET with the black-box NN.

The rest of this article is organized as below. Section II introduces the system model and problem formulation.

TABLE I  
COMPARISON BETWEEN THIS WORK AND THE RELATED ONES

Reference	RIS	Deep unfolding	Optimization variables	Algorithm	Objective function
[15]	w/o	w/o	Transmit waveform	Coordinate descent	Sensing SINR
[16]	w/o	w/o	Transmit waveform	PDD <sup>1</sup> , MM <sup>2</sup> , BCD <sup>3</sup>	Beampattern mismatch
[17]	w/	w/o	Transmit waveform and phase shifts	AO <sup>4</sup> , RCG <sup>5</sup>	WMSCCP <sup>6</sup>
[18]	w/	w/o	Transmit waveform and phase shifts	BCD, ECF <sup>7</sup>	Weighted sum of SINR and MUI energy
[32]	w/o	w/	Precoding matrices	WMMSE	Weighted sum rate
[33]	w/o	w/	Detector coefficients	ADMM	Mean squared error
[34]	w/o	w/	Hybrid beamforming	PGD	Mean squared error
[35]	w/o	w/	Hybrid beamforming	PGD	Sum rate
[36]	w/o	w/	Transmit waveform	PGD	WSMEWD <sup>8</sup>
Our work	w/	w/	Transmit waveform and phase shifts	ADMM	WSMEWD

<sup>1</sup>PDD: penalty dual decomposition, <sup>2</sup>MM: majorization-minimization, <sup>3</sup>BCD: block coordinate descent, <sup>4</sup>AO: alternating optimization, <sup>5</sup>RCG: Riemannian conjugate gradient, <sup>6</sup>WMSCCP: weighted mean square cross-correlation pattern, <sup>7</sup>ECF: element-wise closed-form, <sup>8</sup>WSMEWD: weighted sum of MUI energy and waveform discrepancy.

Sections III and IV present the proposed ADMM-based iterative algorithm and deep unfolding NN for the investigated optimization problem, respectively. Section V provides simulation results with the conclusion in Section VI.

*Notation:*  $|\cdot|$ ,  $\|\cdot\|_2$  and  $\|\cdot\|_F$  represent the modulus,  $\ell_2$  norm and Frobenius norm, respectively.  $(\cdot)^T$ ,  $(\cdot)^H$  and  $(\cdot)^{-1}$  stand for the transpose, conjugate transpose and inverse, respectively.  $j$  and  $\otimes$  denote the imaginary unit and Kronecker product, respectively.  $\mathcal{CN}(\mathbf{v}, \Sigma)$  denotes the circularly symmetric complex Gaussian distribution with mean  $\mathbf{v}$  and covariance matrix  $\Sigma$ .  $\text{diag}(\mathbf{x})$  represents a matrix whose diagonal elements are made up of  $\mathbf{x}$ .  $\text{vec}(\mathbf{X})$  transforms  $\mathbf{X}$  to a column vector in a column-first manner.  $\angle \cdot$  represents the angle of a complex number, and  $\mathbf{A}(m, n)$  denotes the  $(m, n)$ th element of  $\mathbf{A}$ .  $\partial$  and  $\nabla$  refer to the partial derivative and gradient operations, respectively.

## II. SYSTEM MODEL AND PROBLEM FORMULATION

Consider an RIS-aided ISAC system as illustrated in Fig. 1, where the ISAC-BS with  $N_t$  antennas transmits the DF waveform to sense a specific target and serve  $K$  ( $1 \leq K < N_t$ ) single-antenna users simultaneously. Owing to the severe blockage, there is no direct link from ISAC-BS to users. Therefore, an RIS with  $M$  ( $M > 1$ ) reflection elements is deployed to establish the virtual line-of-sight links between the ISAC-BS and users. The channels from ISAC-BS to RIS and RIS to the  $k$ th user can be formulated as  $\mathbf{H}_{ai} \in \mathbb{C}^{M \times N_t}$  and  $\mathbf{h}_{i,k} \in \mathbb{C}^{M \times 1}$ ,  $k \in \{1, \dots, K\}$ , respectively. The phase shifts at RIS can be given by  $\Phi = \text{diag}(\phi^H) \in \mathbb{C}^{M \times M}$ , where  $\phi(m) = e^{j\varphi_m}$  ( $|\phi(m)| = 1, \forall m$ ) denotes the reflection coefficient of the  $m$ th element. We investigate the long-term waveform design and the whole time is evenly divided into  $L$  time slots [15], [17]. Without loss of generality, the communication channels and the phase shifts at RIS remain identical during the whole time [40].

### A. Signal Model

The received signal at the users during  $L$  time slots can be given by

$$\mathbf{Y} = \mathbf{H}\mathbf{X} + \mathbf{W}, \quad (1)$$

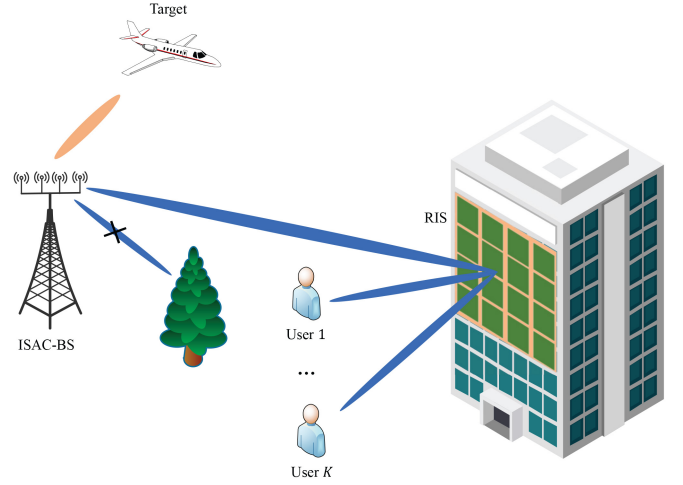


Fig. 1. The RIS-aided ISAC system.

where  $\mathbf{X} = [\mathbf{x}_1, \dots, \mathbf{x}_L] \in \mathbb{C}^{N_t \times L}$  stands for the DF waveform at the ISAC-BS,  $\mathbf{W} = [\mathbf{w}_1, \dots, \mathbf{w}_L] \in \mathbb{C}^{K \times L}$  denotes the noise matrix with  $\mathbf{w}_\ell \sim \mathcal{CN}(\mathbf{0}, \sigma^2 \mathbf{I})$ ,  $\forall \ell \in \{1, \dots, L\}$ ,  $\sigma^2$  represents the noise power, and  $\mathbf{H} = [(\mathbf{h}_{i,1}^H \Phi \mathbf{H}_{ai})^T, \dots, (\mathbf{h}_{i,K}^H \Phi \mathbf{H}_{ai})^T]^T \in \mathbb{C}^{K \times N_t}$  refers to the equivalent channels from the ISAC-BS to users.

Let  $\mathbf{S} \in \mathbb{C}^{K \times L}$  represent the desired communication symbol of users, (1) can be rewritten as

$$\mathbf{Y} = \mathbf{S} + \underbrace{(\mathbf{H}\mathbf{X} - \mathbf{S})}_{\text{MUI}} + \mathbf{W}, \quad (2)$$

where the term  $(\mathbf{H}\mathbf{X} - \mathbf{S})$  stands for the MUI.

Therefore, for the  $k$ th user, its SINR per time slot can be written as [15]

$$\gamma_k = \frac{\mathbb{E}(|\mathbf{S}(k, \ell)|^2)}{\underbrace{\mathbb{E}(|\mathbf{h}_{i,k}^H \Phi \mathbf{H}_{ai} \mathbf{x}_\ell - \mathbf{S}(k, \ell)|^2)}_{\text{MUI energy}} + \sigma^2}, \forall k, \ell, \quad (3)$$

where  $\mathbb{E}(\cdot)$  represents the mathematical expectation. We can observe from (3) that, for the given  $\mathbf{S}$  with constant power,  $\gamma_k$  can be maximized via minimizing the MUI energy. Consequently, we adopt the MUI energy as the communication performance metric.

To obtain the satisfactory sensing performance, the transmitted waveform should exhibit the properties of good autocorrelation and high peak-to-sidelobe ratio. Nevertheless, it may be difficult to directly optimize the DF waveform with satisfactory sensing capability. As a remedy, the traditional sensing waveforms, such as the frequency modulated continuous wave (FMCW) waveform, can be utilized as a reference. In addition, the sensing performance of DF waveform can be evaluated by the waveform discrepancy as

$$\|\mathbf{X} - \mathbf{X}_0\|_F^2, \quad (4)$$

where  $\mathbf{X}_0$  denotes the reference FMCW waveform given by

$$\mathbf{X}_0 = \sqrt{\frac{P}{N_t L}} \mathbf{a}(\theta_0) \tilde{\mathbf{x}}^H. \quad (5)$$

In (5),  $P$  denotes the transmit power,  $\theta_0$  stands for the angle of target,  $\mathbf{a}(\theta_0) = [1, e^{j\pi \sin \theta_0}, \dots, e^{j\pi(N_t-1) \sin \theta_0}]^T \in \mathbb{C}^{N_t \times 1}$  refers to the steering vector towards the target,  $\tilde{\mathbf{x}} = [\tilde{\mathbf{x}}(1), \dots, \tilde{\mathbf{x}}(L)]^T \in \mathbb{C}^{L \times 1}$  denotes the FMCW waveform with  $\tilde{\mathbf{x}}(\ell) = e^{j2\pi(\frac{f_0}{f_s}\ell + \frac{\nu}{f_s^2}\ell^2)}$ ,  $f_s$  represents the sampling frequency,  $\nu$  denotes the chirp rate, and  $f_0$  refers to the carrier frequency.

It can be observed that the smaller  $\|\mathbf{X} - \mathbf{X}_0\|_F$  is, the better sensing performance will be. Moreover, the transmitted beampattern towards angle  $\vartheta$  can be given by

$$P_d(\vartheta) = \frac{1}{L} \mathbf{a}^H(\vartheta) (\mathbf{X} \mathbf{X}^H) \mathbf{a}(\vartheta), \vartheta \in \left[-\frac{\pi}{2}, \frac{\pi}{2}\right], \quad (6)$$

where  $\mathbf{a}(\vartheta) = [1, e^{j\pi \sin \vartheta}, \dots, e^{j\pi(N_t-1) \sin \vartheta}]^T$  denotes the steering vector corresponding to  $\vartheta$ .

### B. Problem Formulation

We aim at obtaining a DF waveform for the RIS-aided ISAC system. Similar to [15], the WSMED is minimized via jointly optimizing the DF waveform at the ISAC-BS and phase shifts at the RIS to keep a good balance between the two functionalities, yielding the joint optimization problem as

$$\min_{\mathbf{X}, \Phi} \rho \|\mathbf{H} \mathbf{X} - \mathbf{S}\|_F^2 + (1 - \rho) \|\mathbf{X} - \mathbf{X}_0\|_F^2 \quad (7a)$$

$$s.t. \quad \|\mathbf{X}\|_F^2 = P, \quad (7b)$$

$$|\Phi(i, i)| = 1, \forall i \in \{1, \dots, M\}, \quad (7c)$$

where  $\rho \in [0, 1]$  denotes the weighting coefficient, (7b) stands for the transmit power constraint, and (7c) denotes the constant modulus constraint. However, (7) is non-convex due to the non-convex constraints and coupled variables.

In order to deal with this issue, we first tackle (7) via the proposed ADMM-based iterative algorithm in Section III. In Section IV, to reduce the computational complexity and facilitate the online deployment, we design a model-driven NN via unfolding the proposed ADMM-based iterative algorithm.

### III. ADMM-BASED ITERATIVE ALGORITHM

In this section, we propose an ADMM-based iterative algorithm to deal with (7). Specifically, the original problem is first decomposed into four subproblems and then these subproblems are alternately optimized. Furthermore, the closed-form solution to each subproblem is derived.

#### A. Problem Reformulation

Let  $\mathbf{x} \triangleq \text{vec}(\mathbf{X})$ , and the term  $\|\mathbf{H} \mathbf{X} - \mathbf{S}\|_F^2$  can be equivalently formulated as

$$\|\mathbf{H} \mathbf{X} - \mathbf{S}\|_F^2 = \sum_{k=1}^K \left\| \left( \mathbf{h}_{i,k}^H \Phi \mathbf{H}_{ai} \right) \mathbf{x} - \mathbf{s}_k \right\|_2^2, \quad (8a)$$

$$= \sum_{k=1}^K \left\| \phi^H \tilde{\mathbf{H}}_{a,k} \mathbf{x} - \mathbf{s}_k \right\|_2^2, \quad (8b)$$

$$= \sum_{k=1}^K \left\| \left[ \phi^H \tilde{\mathbf{H}}_{a,k} \mathbf{x}_1, \dots, \phi^H \tilde{\mathbf{H}}_{a,k} \mathbf{x}_L \right] - \mathbf{s}_k \right\|_2^2, \quad (8c)$$

$$= \sum_{k=1}^K \left\| \begin{bmatrix} \phi^H \tilde{\mathbf{H}}_{a,k} \mathbf{x}_1 \\ \vdots \\ \phi^H \tilde{\mathbf{H}}_{a,k} \mathbf{x}_L \end{bmatrix} - \begin{bmatrix} \mathbf{s}_k(1) \\ \vdots \\ \mathbf{s}_k(L) \end{bmatrix} \right\|_2^2, \quad (8d)$$

$$= \sum_{k=1}^K \left\| \left( \mathbf{I}_L \otimes (\phi^H \tilde{\mathbf{H}}_{a,k}) \right) \mathbf{x} - \mathbf{s}_k^T \right\|_2^2, \quad (8e)$$

where  $\tilde{\mathbf{H}}_{a,k} \triangleq \text{diag}(\mathbf{h}_{i,k}^H) \mathbf{H}_{ai} \in \mathbb{C}^{M \times N_t}$ ,  $\mathbf{s}_k \in \mathbb{C}^{1 \times L}$  represents the  $k$ th row of  $\mathbf{S}$ , and  $\mathbf{I}_L \in \mathbb{R}^{L \times L}$  stands for an  $L$ -dimension identity matrix.

Therefore, (7) can be equivalently formulated as

$$\min_{\mathbf{x}, \phi} \rho \sum_{k=1}^K \left\| \left( \mathbf{I}_L \otimes (\phi^H \tilde{\mathbf{H}}_{a,k}) \right) \mathbf{x} - \mathbf{s}_k^T \right\|_2^2 + (1 - \rho) \|\mathbf{x} - \mathbf{x}_0\|_2^2 \quad (9a)$$

$$s.t. \quad \mathbf{x}^H \mathbf{x} = P, \quad (9b)$$

$$|\phi(i)| = 1, \forall i \in \{1, \dots, M\}, \quad (9c)$$

which is still non-convex.

By introducing the slack variable  $\omega \in \mathbb{R}^{M \times 1}$ , (9) can be equivalently rewritten as

$$\min_{\mathbf{x}, \phi, \omega} \rho \sum_{k=1}^K \left\| \left( \mathbf{I}_L \otimes (\phi^H \tilde{\mathbf{H}}_{a,k}) \right) \mathbf{x} - \mathbf{s}_k^T \right\|_2^2 + (1 - \rho) \|\mathbf{x} - \mathbf{x}_0\|_2^2 \quad (10a)$$

$$s.t. \quad \mathbf{x}^H \mathbf{x} = P, \quad (10b)$$

$$\phi = e^{j\omega}. \quad (10c)$$

The scaled augmented Lagrangian function of the objective function in (10) can be formulated as

$$\begin{aligned} \mathcal{L}_\mu(\mathbf{x}, \phi, \omega, \mathbf{v}) = & \rho \sum_{k=1}^K \left\| \left( \mathbf{I}_L \otimes (\phi^H \tilde{\mathbf{H}}_{a,k}) \right) \mathbf{x} - \mathbf{s}_k^T \right\|_2^2 \\ & + (1 - \rho) \|\mathbf{x} - \mathbf{x}_0\|_2^2 + \frac{\mu}{2} \left( \|\phi - e^{j\omega} + \mathbf{v}\|_2^2 - \|\mathbf{v}\|_2^2 \right), \end{aligned} \quad (11)$$

where  $\mathbf{v} \in \mathbb{C}^{M \times 1}$  refers to a slack variable, and  $\mu (\mu > 0)$  represents a penalty coefficient.

Therefore, the augmented Lagrangian problem of (10) can be formulated as

$$\min_{\mathbf{x}, \phi, \omega, \mathbf{v}} \mathcal{L}_\mu(\mathbf{x}, \phi, \omega, \mathbf{v}) \quad (12a)$$

$$s.t. \quad (10c). \quad (12b)$$



We propose an ADMM-based algorithm to deal with (12), which alternatively optimizes each optimization variable and the  $t$ th iteration of it is composed of the following steps:

$$\mathbf{x}^{t+1} = \arg \min_{\mathbf{x}} \mathcal{L}_{\mu}(\mathbf{x}, \boldsymbol{\phi}^t, \boldsymbol{\omega}^t, \mathbf{v}^t) \quad (13a)$$

$$s.t. \quad (10b),$$

$$\boldsymbol{\phi}^{t+1} = \arg \min_{\boldsymbol{\phi}} \mathcal{L}_{\mu}(\mathbf{x}^{t+1}, \boldsymbol{\phi}, \boldsymbol{\omega}^t, \mathbf{v}^t) \quad (13b)$$

$$\boldsymbol{\omega}^{t+1} = \angle(\boldsymbol{\phi}^{t+1} + \mathbf{v}^t), \quad (13c)$$

$$\mathbf{v}^{t+1} = \mathbf{v}^t + \boldsymbol{\phi}^{t+1} - e^{j\boldsymbol{\omega}^{t+1}}. \quad (13d)$$

### B. Waveform Optimization

With given  $\boldsymbol{\phi}^t$ ,  $\boldsymbol{\omega}^t$  and  $\mathbf{v}^t$ , (13a) can be equivalently written as

$$\min_{\mathbf{x}} \rho \sum_{k=1}^K \left\| \left( \mathbf{I}_L \otimes (\boldsymbol{\phi}^{t,H} \tilde{\mathbf{H}}_{a,k}) \right) \mathbf{x} - \mathbf{s}_k^T \right\|_2^2 + (1 - \rho) \|\mathbf{x} - \mathbf{x}_0\|_2^2 \quad (14a)$$

$$s.t. \quad (10b), \quad (14b)$$

whose Lagrangian function can be given by

$$\mathcal{L}_{\mathbf{x}}(\mathbf{x}, \lambda) = \rho \sum_{k=1}^K \left\| \left( \mathbf{I}_L \otimes (\boldsymbol{\phi}^{t,H} \tilde{\mathbf{H}}_{a,k}) \right) \mathbf{x} - \mathbf{s}_k^T \right\|_2^2 + (1 - \rho) \|\mathbf{x} - \mathbf{x}_0\|_2^2 + \lambda (\mathbf{x}^H \mathbf{x} - P), \quad (15)$$

where  $\lambda$  stands for the Lagrangian multiplier.

According to the Karush-Kuhn-Tucker (KKT) condition, we have

$$\frac{\partial \mathcal{L}_{\mathbf{x}}(\mathbf{x}, \lambda)}{\partial \mathbf{x}} = 2\rho \sum_{k=1}^K \mathbf{A}_k^{t,H} (\mathbf{A}_k^t \mathbf{x} - \mathbf{s}_k^T) + 2(1 - \rho)(\mathbf{x} - \mathbf{x}_0) + 2\lambda \mathbf{x} = \mathbf{0}, \quad (16)$$

where  $\mathbf{A}_k^t = \mathbf{I}_L \otimes (\boldsymbol{\phi}^{t,H} \tilde{\mathbf{H}}_{a,k}) \in \mathbb{C}^{L \times LN_t}$ ,  $k \in \{1, \dots, K\}$ .

By solving (16),  $\mathbf{x}^{t+1}$  can be given by (17) shown at the bottom of the page. The closed-form solution of  $\mathbf{x}$  can be regarded as the weighted sum of communication related term

and reference waveform related term, and  $\rho$  stands for the weighted coefficient. Without loss of generality,  $\lambda$  can be set to 0 and  $\mathbf{x}$  can be normalized to satisfy the constraint (10b) as solution in (18) shown at the bottom of the page.

### C. Phase-Shift Optimization

With given  $\mathbf{x}^{t+1}$ ,  $\boldsymbol{\omega}^t$  and  $\mathbf{v}^t$ , (13b) can be equivalently written as

$$\min_{\boldsymbol{\phi}} \rho \sum_{k=1}^K \left\| \left( \mathbf{I}_L \otimes (\boldsymbol{\phi}^H \tilde{\mathbf{H}}_{a,k}) \right) \mathbf{x}^{t+1} - \mathbf{s}_k^T \right\|_2^2 + \frac{\mu}{2} \left\| \boldsymbol{\phi} - e^{j\boldsymbol{\omega}^t} + \mathbf{v}^t \right\|_2^2, \quad (19)$$

where the objective function is very complicated with respect to (w.r.t.)  $\boldsymbol{\phi}$  owing to the intractable operations, such as the Kronecker product. Towards this difficulty, we derive its closed-form solution in Lemma 1.

**Lemma 1:** The optimal solution to (19) can be formulated as (20) shown at the bottom of the page, where  $\mathbf{c}_k^{t+1} = (\mathbf{I}_L \otimes \tilde{\mathbf{H}}_{a,k}) \mathbf{x}^{t+1} = [\mathbf{c}_{k,1}^{t+1,T}, \dots, \mathbf{c}_{k,L}^{t+1,T}]^T \in \mathbb{C}^{LM \times 1}$ ,  $k \in \{1, \dots, K\}$ , and  $\mathbf{c}_{k,l}^{t+1} \in \mathbb{C}^{M \times 1}$ ,  $\forall l \in \{1, \dots, L\}$ . It can be seen from (20) that  $\boldsymbol{\phi}^{t+1}$  is the weighted sum of communication symbols related term and constant modulus constraint related term.

**Proof:** Via necessary mathematical manipulation, the term  $\|(\mathbf{I}_L \otimes (\boldsymbol{\phi}^H \tilde{\mathbf{H}}_{a,k})) \mathbf{x}^{t+1} - \mathbf{s}_k^T\|_2^2$  can be equivalently formulated as

$$\left\| \left( \mathbf{I}_L \otimes (\boldsymbol{\phi}^H \tilde{\mathbf{H}}_{a,k}) \right) \mathbf{x}^{t+1} - \mathbf{s}_k^T \right\|_2^2 \quad (21a)$$

$$= \left\| \left( (\mathbf{I}_L \mathbf{I}_L) \otimes (\boldsymbol{\phi}^H \tilde{\mathbf{H}}_{a,k}) \right) \mathbf{x}^{t+1} - \mathbf{s}_k^T \right\|_2^2, \quad (21b)$$

$$\stackrel{(a)}{=} \left\| \left( \mathbf{I}_L \otimes \boldsymbol{\phi}^H \right) \left( \mathbf{I}_L \otimes \tilde{\mathbf{H}}_{a,k} \right) \mathbf{x}^{t+1} - \mathbf{s}_k^T \right\|_2^2, \quad (21c)$$

$$= \left\| \left( \mathbf{I}_L \otimes \boldsymbol{\phi}^H \right) \mathbf{c}_k^{t+1} - \mathbf{s}_k^T \right\|_2^2, \quad (21d)$$

where (a) holds due to  $(\mathbf{AB}) \otimes (\mathbf{CD}) = (\mathbf{A} \otimes \mathbf{C})(\mathbf{B} \otimes \mathbf{D})$ , and  $\mathbf{c}_k^{t+1} = (\mathbf{I}_L \otimes \tilde{\mathbf{H}}_{a,k}) \mathbf{x}^{t+1} \in \mathbb{C}^{LM \times 1}$ ,  $k \in \{1, \dots, K\}$  [41].

In addition, the term  $\|(\mathbf{I}_L \otimes \boldsymbol{\phi}^H) \mathbf{c}_k^{t+1} - \mathbf{s}_k^T\|_2^2$  can be equivalently written as

$$\mathbf{x}^{t+1} = \left( \rho \sum_{k=1}^K \mathbf{A}_k^{t,H} \mathbf{A}_k^t + (1 - \rho) \mathbf{I} + \lambda \mathbf{I} \right)^{-1} \left( \rho \sum_{k=1}^K \mathbf{A}_k^{t,H} \mathbf{s}_k^T + (1 - \rho) \mathbf{x}_0 \right). \quad (17)$$

$$\mathbf{x}^{t+1} = \frac{\sqrt{P} \left( \rho \sum_{k=1}^K \mathbf{A}_k^{t,H} \mathbf{A}_k^t + (1 - \rho) \mathbf{I} \right)^{-1} \left( \rho \sum_{k=1}^K \mathbf{A}_k^{t,H} \mathbf{s}_k^T + (1 - \rho) \mathbf{x}_0 \right)}{\left\| \left( \rho \sum_{k=1}^K \mathbf{A}_k^{t,H} \mathbf{A}_k^t + (1 - \rho) \mathbf{I} \right)^{-1} \left( \rho \sum_{k=1}^K \mathbf{A}_k^{t,H} \mathbf{s}_k^T + (1 - \rho) \mathbf{x}_0 \right) \right\|_2}. \quad (18)$$

$$\boldsymbol{\phi}^{t+1} = \left( 2\rho \sum_{k=1}^K \sum_{l=1}^L \mathbf{c}_{k,l}^{t+1} \mathbf{c}_{k,l}^{t+1,H} + \mu \mathbf{I} \right)^{-1} \left( 2\rho \sum_{k=1}^K \sum_{l=1}^L \mathbf{c}_{k,l}^{t+1} \mathbf{s}_k^*(l) + \mu \left( e^{j\boldsymbol{\omega}^t} - \mathbf{v}^t \right) \right). \quad (20)$$

**Algorithm 1** ADMM-Based Iterative Algorithm for (7)

- 1: Initialization: Set an initial point  $(\mathbf{x}^0, \boldsymbol{\phi}^0, \boldsymbol{\omega}^0, \mathbf{v}^0)$ , the index of iteration  $t = 0$  and convergence accuracy  $\epsilon$ .
- 2: **repeat**
- 3:   With given  $(\boldsymbol{\phi}^t, \boldsymbol{\omega}^t, \mathbf{v}^t)$ , obtain  $\mathbf{x}^{t+1}$  from (18).
- 4:   With given  $(\mathbf{x}^{t+1}, \boldsymbol{\omega}^t, \mathbf{v}^t)$ , obtain  $\boldsymbol{\phi}^{t+1}$  from (20).
- 5:   With given  $(\mathbf{x}^{t+1}, \boldsymbol{\phi}^{t+1}, \mathbf{v}^t)$ , obtain  $\boldsymbol{\omega}^{t+1}$  from (13c).
- 6:   With given  $(\mathbf{x}^{t+1}, \boldsymbol{\phi}^{t+1}, \boldsymbol{\omega}^{t+1})$ , obtain  $\mathbf{v}^{t+1}$  from (13d).
- 7:    $t \leftarrow t + 1$ .
- 8: **until**  $|\mathcal{L}_\mu(\mathbf{x}^{t+1}, \boldsymbol{\phi}^{t+1}, \boldsymbol{\omega}^{t+1}, \mathbf{v}^{t+1}) - \mathcal{L}_\mu(\mathbf{x}^t, \boldsymbol{\phi}^t, \boldsymbol{\omega}^t, \mathbf{v}^t)| \leq \epsilon$ .
- 9: **Output:**  $(\mathbf{x}^{t+1}, \boldsymbol{\phi}^{t+1}, \boldsymbol{\omega}^{t+1}, \mathbf{v}^{t+1})$ .

$$\|(\mathbf{I}_L \otimes \boldsymbol{\phi}^H) \mathbf{c}_k^{t+1} - \mathbf{s}_k^T\|_2^2 \quad (22a)$$

$$= \left\| \begin{bmatrix} \boldsymbol{\phi}^H & & \\ & \ddots & \\ & & \boldsymbol{\phi}^H \end{bmatrix} \begin{bmatrix} \mathbf{c}_{k,1}^{t+1} \\ \vdots \\ \mathbf{c}_{k,L}^{t+1} \end{bmatrix} - \mathbf{s}_k^T \right\|_2^2, \quad (22b)$$

$$= \left\| \begin{bmatrix} \boldsymbol{\phi}^H \mathbf{c}_{k,1}^{t+1} \\ \vdots \\ \boldsymbol{\phi}^H \mathbf{c}_{k,L}^{t+1} \end{bmatrix} - \begin{bmatrix} s_k(1) \\ \vdots \\ s_k(L) \end{bmatrix} \right\|_2^2, \quad (22c)$$

$$= \sum_{l=1}^L |\boldsymbol{\phi}^H \mathbf{c}_{k,l}^{t+1} - s_k(l)|^2, \quad (22d)$$

where  $\mathbf{c}_k^{t+1} = (\mathbf{I}_L \otimes \tilde{\mathbf{H}}_{a,k}) \mathbf{x}^{t+1} = [\mathbf{c}_{k,1}^{t+1,T}, \dots, \mathbf{c}_{k,L}^{t+1,T}]^T$ , and  $\mathbf{c}_{k,l}^{t+1} \in \mathbb{C}^{M \times 1}$ ,  $\forall l \in \{1, \dots, L\}$ .

Consequently, (13b) can be equivalently formulated as

$$\min_{\boldsymbol{\phi}} \tilde{\mathcal{L}}_\mu(\mathbf{x}^{t+1}, \boldsymbol{\phi}, \boldsymbol{\omega}^t, \mathbf{v}^t), \quad (23)$$

where  $\tilde{\mathcal{L}}_\mu(\mathbf{x}^{t+1}, \boldsymbol{\phi}, \boldsymbol{\omega}^t, \mathbf{v}^t) \triangleq \rho \sum_{k=1}^K \sum_{l=1}^L |\boldsymbol{\phi}^H \mathbf{c}_{k,l}^{t+1} - s_k(l)|^2 + \frac{\mu}{2} \|\boldsymbol{\phi} - e^{j\boldsymbol{\omega}^t} + \mathbf{v}^t\|_2^2$ . Since (23) is an unconstrained optimization problem, according to the first-order optimality condition, the optimal  $\boldsymbol{\phi}^{t+1}$  should satisfy

$$\frac{\partial \tilde{\mathcal{L}}_\mu(\mathbf{x}^{t+1}, \boldsymbol{\phi}, \boldsymbol{\omega}^t, \mathbf{v}^t)}{\partial \boldsymbol{\phi}} = 2\rho \sum_{k=1}^K \sum_{l=1}^L \mathbf{c}_{k,l}^{t+1} (\mathbf{c}_{k,l}^{t+1,H} \boldsymbol{\phi} - \mathbf{s}_k^*(l)) + \mu (\boldsymbol{\phi} - e^{j\boldsymbol{\omega}^t} + \mathbf{v}^t) = \mathbf{0}. \quad (24)$$

By solving (24), the optimal  $\boldsymbol{\phi}^{t+1}$  can be written as (20) at the top of next page. ■

**D. Algorithm Analysis**

The proposed ADMM-based iterative algorithm for (7) is presented in Algorithm 1, which first decomposes the original problem into four subproblems to be optimized alternatively. Moreover, we derive the closed-form solution to each subproblem. It can be seen that the computational complexity is mainly determined by the matrix multiplication and inversion involved in (18) and (20). Specifically, the computational complexities

of updating  $\mathbf{x}$  and  $\boldsymbol{\phi}$  in each iteration can be formulated as  $\mathcal{O}(L^3 N_t^3 + L^3 N_t^2 + L^2 K N_t)$  and  $\mathcal{O}(M^3 + M^2 K L + L^2 N_t M)$ , respectively. Consequently, the computational complexity of Algorithm 1 can be approximately given by

$$\mathcal{O}\left(I_1 \left(L^3 N_t^3 + L^2 K N_t + M^3 + M^2 K L + L^2 N_t M\right)\right), \quad (25)$$

where  $I_1$  refers to the number of iterations.

According to [42], ADMM exhibits the superior convergence property. Therefore, the proposed ADMM-based iterative algorithm guarantees to converge, which is also verified by the simulation results in Section V.

**IV. DEEP UNFOLDING NN: ADMM-NET**

Although the proposed ADMM-based iterative algorithm can deal with (7), it encounters the drawback of high computational complexity, hindering the online deployment. In this section, we develop a low-complexity deep unfolding NN, named ADMM-NET, to tackle (7) via unfolding the proposed ADMM-based iterative algorithm to a layer-wise architecture. Subsequently, a black-box NN with supervised learning and unsupervised learning is also proposed as a benchmark. Finally, we compare the proposed ADMM-NET and its black-box counterpart.

**A. ADMM-NET Based on Deep Unfolding**

Since the computational complexity of matrix inversion is very high, especially when the dimension is large, we adopt the low-complexity approximation in [43] for complexity reduction. Specifically, for an invertible matrix  $\mathbf{E}$ ,  $\mathbf{E}^{-1}$  can be approximately written as  $\mathbf{E}^\ddagger \mathbf{U} + \mathbf{E} \mathbf{Y} + \mathbf{Z}$ , where  $\mathbf{U}$ ,  $\mathbf{Y}$  and  $\mathbf{Z}$  are the learnable parameters.  $\mathbf{E}^\ddagger$  represents a non-linear operation, which takes the reciprocal of each diagonal entry of  $\mathbf{E}$  and sets the off-diagonal entries as zero. Taking a  $3 \times 3$  matrix  $\tilde{\mathbf{E}}$ , whose  $(i, j)$ th element is  $e_{i,j}$  ( $e_{i,j} \neq 0, \forall i, j \in \{1, 2, 3\}$ ), as an example,  $\tilde{\mathbf{E}}^\ddagger$  can be formulated as

$$\tilde{\mathbf{E}}^\ddagger = \begin{bmatrix} \frac{1}{e_{1,1}} & 0 & 0 \\ 0 & \frac{1}{e_{2,2}} & 0 \\ 0 & 0 & \frac{1}{e_{3,3}} \end{bmatrix}. \quad (26)$$

Accordingly, the update of  $\mathbf{x}$  and  $\boldsymbol{\phi}$  in the  $m$ th iteration can be approximately formulated as (27) shown at the bottom of the page, where the set  $\Omega^{m-1} \triangleq \{\mathbf{U}_x^{m-1}, \mathbf{Y}_x^{m-1}, \mathbf{Z}_x^{m-1}\} \cup \{\mathbf{U}_\phi^{m-1}, \mathbf{Y}_\phi^{m-1}, \mathbf{Z}_\phi^{m-1}\}$  contains several learnable parameters to approximate the inverse matrices  $\tilde{\mathbf{A}}^{m-1,-1} \triangleq (\rho \sum_{k=1}^K \mathbf{A}_k^{m-1,H} \mathbf{A}_k^{m-1} + (1 - \rho) \mathbf{I})^{-1}$  and  $\tilde{\mathbf{B}}^{m-1,-1} \triangleq (2\rho \sum_{k=1}^K \sum_{l=1}^L \mathbf{c}_{k,l}^m \mathbf{c}_{k,l}^{m,H} + \mu \mathbf{I})^{-1}$ , respectively. In addition,  $\{\mathbf{O}_x^{m-1}, \mathbf{O}_\phi^{m-1}\}$  stands for the learnable offsets.<sup>1</sup>

The architecture of ADMM-NET is illustrated in Fig. 2, which follows the processing procedure of the proposed ADMM-based iterative algorithm, and the  $m$ th layer consists of four computing units  $\tilde{\mathbf{x}}^m$ ,  $\tilde{\boldsymbol{\phi}}^m$ ,  $\tilde{\boldsymbol{\omega}}^m$  and  $\tilde{\mathbf{v}}^m$ . The computations involved in  $\tilde{\mathbf{x}}^m$  and  $\tilde{\boldsymbol{\phi}}^m$  are presented in (27a)

<sup>1</sup>In practice, the complex number operations are equivalently converted to real number operations because existing deep learning frameworks, such as PyTorch, generally prefer real number operations [35].

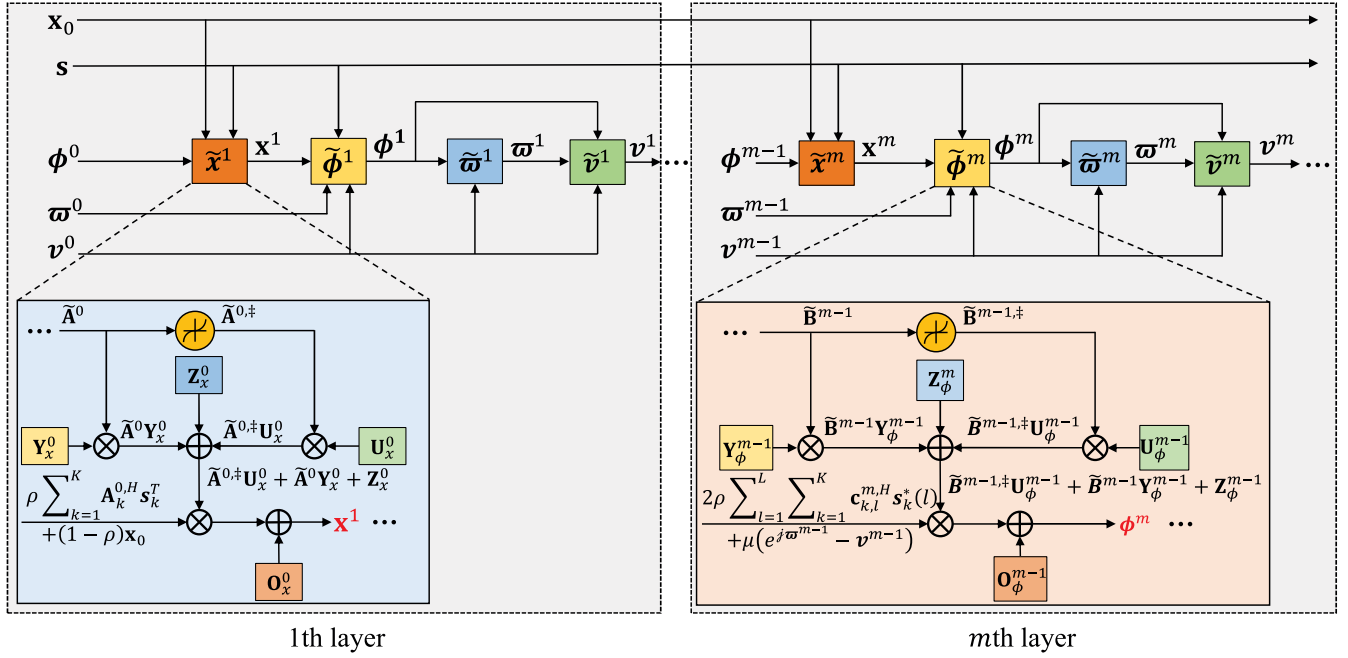


Fig. 2. Architecture of ADMM-NET.

and (27b) shown at the bottom of the page, respectively. In addition, (13c) and (13d) provide the formulations contained in  $\tilde{\omega}^m$  and  $\tilde{v}^m$ , respectively. Consequently, all the learnable parameters involved in ADMM-NET can be given by  $\Xi = \bigcup_{m=1}^{I_n} \Omega^m \cup \{\mathbf{O}_x^m, \mathbf{O}_\phi^m\}$ , where  $I_n$  refers to the number of hidden layers. It can be observed that each iteration of ADMM-based iterative algorithm is unfolded to each layer with introduced learnable parameters of ADMM-NET. The benefits of the introduced learnable parameters are two-fold.<sup>2</sup> On the one hand, these learnable parameters are utilized to approximate the high-complexity operations. On the other hand, more learnable parameters can enhance the non-linear fitting capability of NNs.

Owing to the inherent non-convexity, it is difficult to obtain the globally optimal solution to (7). Although the obtained sub-optimal solution by the ADMM-based iterative algorithm can be acted as the training label, this approach may limit the performance of ADMM-NET because the ADMM-based iterative algorithm serves as an upper bound. Consequently, ADMM-NET is trained in an unsupervised learning manner to explore a higher quality solution. In the training stage, a fixed number of samples are fed into the ADMM-NET to enhance the efficiency. The training procedure of ADMM-NET is presented in Algorithm 2. In particular, the ADMM-NET

<sup>2</sup>Note that increasing the number of the learnable parameters requires more samples to fine tune.

is trained with the data set  $\mathcal{D}$  with  $|\mathcal{D}|$  training samples. The parameters of ADMM-NET are first initialized, and then the ADMM-NET is trained over  $\mathcal{E}$  ( $\mathcal{E} > 1$ ) episodes. In each episode, every sample is fed into the ADMM-NET to obtain the corresponding prediction, and then the loss can be calculated according to the specific metric. Finally, the ADMM-NET adjusts its parameters by Adam optimizer to minimize the loss. Although the scaled augmented Lagrangian function in (11) can be utilized as the loss function of ADMM-NET, it cannot guarantee that the objective function value is nonnegative, resulting in training efficiency degradation. To handle this problem, we utilize the modified version of (11) as the loss function of ADMM-NET, expressed as

$$\begin{aligned} \hat{\mathcal{L}}_\mu(\mathbf{x}, \boldsymbol{\phi}, \boldsymbol{\omega}, \mathbf{v}) = & \rho \sum_{k=1}^K \left\| \left( \mathbf{I}_L \otimes (\boldsymbol{\phi}^H \tilde{\mathbf{H}}_{a,k}) \right) \mathbf{x} - \mathbf{s}_k^T \right\|_2^2 \\ & + (1 - \rho) \|\mathbf{x} - \mathbf{x}_0\|_2^2 + \frac{\mu}{2} \left| \left( \|\boldsymbol{\phi} - e^{j\boldsymbol{\omega}} + \mathbf{v}\|_2^2 - \|\mathbf{v}\|_2^2 \right) \right|, \end{aligned} \quad (28)$$

which is nonnegative and  $\frac{\mu}{2} |\left( \|\boldsymbol{\phi} - e^{j\boldsymbol{\omega}} + \mathbf{v}\|_2^2 - \|\mathbf{v}\|_2^2 \right)|$  can be regarded as the regularization term to enhance the training efficiency. When the algorithm converges, (28) is a good approximation of (11) because  $\|\boldsymbol{\phi} - e^{j\boldsymbol{\omega}} + \mathbf{v}\|_2^2 - \|\mathbf{v}\|_2^2$  is approximately equal to zero. Since the loss function of ADMM-NET is the weighted sum of multi-user energy and waveform discrepancy, the ADMM-NET can allow for

$$\mathbf{x}^m = \left( \tilde{\mathbf{A}}^{m-1, \ddagger} \mathbf{U}_x^{m-1} + \tilde{\mathbf{A}}^{m-1} \mathbf{Y}_x^{m-1} + \mathbf{Z}_x^{m-1} \right) \left( \rho \sum_{k=1}^K \mathbf{A}_k^{m-1, H} \mathbf{s}_k^T + (1 - \rho) \mathbf{x}_0 \right) + \mathbf{O}_x^{m-1}, \quad (27a)$$

$$\boldsymbol{\phi}^m = \left( \tilde{\mathbf{B}}^{m-1, \ddagger} \mathbf{U}_\phi^{m-1} + \tilde{\mathbf{B}}^{m-1} \mathbf{Y}_\phi^{m-1} + \mathbf{Z}_\phi^{m-1} \right) \left( 2\rho \sum_{k=1}^K \sum_{l=1}^L \mathbf{c}_{k,l}^m \mathbf{s}_k^*(l) + \mu (e^{j\boldsymbol{\omega}^{m-1}} - \mathbf{v}^{m-1}) \right) + \mathbf{O}_\phi^{m-1}. \quad (27b)$$

**Algorithm 2** Training Procedure of ADMM-NET

- 1: **Input:** Data set  $\mathcal{D} = \{\mathbf{H}^{(i)}, \{\mathbf{h}_{ik}^{(i)}\}, \mathbf{x}_0^{(i)}, \mathbf{S}^{(i)}\}_{i=1}^{|\mathcal{D}|}$  with  $|\mathcal{D}|$  samples and preset the hyperparameters and initial point.
- 2: Initialize ADMM-NET parameter  $\Xi^{(0,0)}$ .
- 3: **for**  $\tilde{e} = 1$  to  $\mathcal{E}$  **do**
- 4:   **for**  $i = 1$  to  $|\mathcal{D}|$  **do**
- 5:     Feed the  $i$ th sample  $\{\mathbf{H}^{(i)}, \{\mathbf{h}_{ik}^{(i)}\}, \mathbf{x}_0^{(i)}, \mathbf{S}^{(i)}\}$  into the ADMM-NET, obtaining the output  $\{\tilde{\mathbf{x}}^{(i)}, \tilde{\boldsymbol{\phi}}^{(i)}, \tilde{\boldsymbol{\omega}}^{(i)}, \tilde{\mathbf{v}}^{(i)}\}$ .
- 6:     Calculate the loss  $\hat{\mathcal{L}}_{\mu}(\tilde{\mathbf{x}}^{(i)}, \tilde{\boldsymbol{\phi}}^{(i)}, \tilde{\boldsymbol{\omega}}^{(i)}, \tilde{\mathbf{v}}^{(i)})$  from (28).
- 7:     Update the network parameter  $\Xi^{(\tilde{e},i)}$  from (29).
- 8:   **end for**
- 9: **end for**
- 10: **Output:** Optimized parameter  $\Xi^{(\mathcal{E},|\mathcal{D}|)}$ .

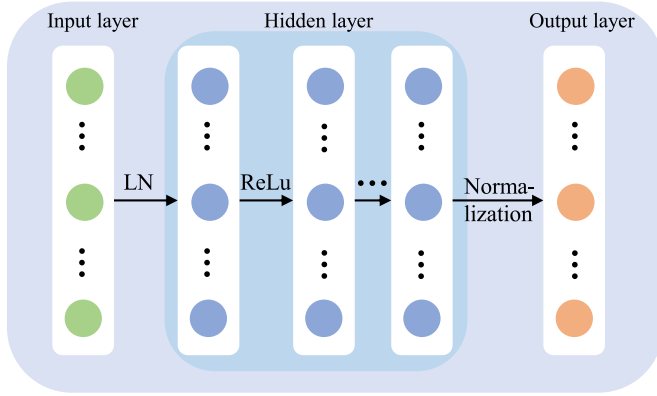


Fig. 3. Architecture of the designed black-box NN.

simultaneous optimization of sensing and communication performance metrics within a single deep learning model.

Accordingly, the update of learnable parameters  $\Xi$  can be formulated as

$$\Xi = \Xi - \eta \nabla_{\Xi} \hat{\mathcal{L}}_{\mu}(\mathbf{x}^{I_n+1}, \boldsymbol{\phi}^{I_n+1}, \boldsymbol{\omega}^{I_n+1}, \mathbf{v}^{I_n+1}), \quad (29)$$

where  $\eta > 0$  denotes the learning rate (LR), and  $\{\mathbf{x}^{I_n+1}, \boldsymbol{\phi}^{I_n+1}, \boldsymbol{\omega}^{I_n+1}, \mathbf{v}^{I_n+1}\}$  represents the output of ADMM-NET.

### B. Black-Box NN

In this subsection, we design a black-box NN as a benchmark, whose architecture is depicted in Fig. 3 at the top of next page, consisting of one input layer, several hidden layers, and one output layer. Each hidden layer contains enormous neurons, and rectified linear unit (ReLU) is utilized as the activation function. The input of NN is the collection of communication channels, desired communication symbols, and reference radar waveform, which can be formulated as  $\mathbf{g} = [\text{vec}(\mathbf{H}_{ai})^T, \mathbf{h}_{i,1}^T, \dots, \mathbf{h}_{i,K}^T, \text{vec}(\mathbf{S})^T, \text{vec}(\mathbf{X}_0)^T]$ . In practice, the input of NN should be real number. Therefore, the real and imaginary parts of  $\mathbf{g}$  are fed into the NN, respectively, and thus the input size of NN is  $2MN_t + 2KL + 2MK + 2N_tL$ . Moreover, before being fed to the NN,  $\mathbf{g}$  is first processed by

layer normalization (LN) to boost the training efficiency and stability. The output of NN is all the optimization variables, i.e.,  $\mathbf{f} = [\mathbf{x}^T, \boldsymbol{\phi}^T]$ . To satisfy the constraints (7b) and (7c), we conduct the normalization on  $\mathbf{f}$  as

$$\mathbf{x} = \sqrt{P} \frac{\mathbf{x}}{\|\mathbf{x}\|_2}, \quad (30a)$$

$$\boldsymbol{\phi} = \angle \boldsymbol{\phi}, \quad (30b)$$

respectively.

To unleash the potential of NN, both supervised learning and unsupervised learning are investigated as following.

1) *Supervised Learning:* For supervised learning, the NN is trained by the labeled samples to learn the mapping from input samples to the corresponding labels. Therefore, for the optimization problem at hand, the globally optimal solutions to the input problem instances can be acted as the training labels. Nevertheless, it is usually difficult to obtain globally optimal solutions to the formulated optimization problem owing to the inherent non-convexity. As a remedy, the obtained high-quality sub-optimal solutions by the ADMM-based iterative algorithm can be utilized as training labels. Moreover, the loss function can be denoted as the mean square error (MSE) between the outputs of NN and training labels.

2) *Unsupervised Learning:* For unsupervised learning, its purpose is often to automatically extract the feature of unlabeled training samples, bypassing the acquisition of manual labels. Moreover, the objective function in (7) can be used as the loss function of NN due to the natural minimization and nonnegativity.

### C. Complexity and Parameter Analysis

According to [43], the computational complexity of ADMM-NET is  $\mathcal{O}(I_n(L^{2.37}N_t^{2.37} + L^2KN_t + M^{2.37} + M^2KL + L^2N_tM))$ . On the one hand, the number of layers in ADMM-NET is much smaller than the iteration number of ADMM-based iterative algorithm, i.e.,  $I_n \ll I_1$ . On the other hand, the high-complexity matrix inversion can be approximated by the low-complex matrix multiplication. Consequently, the ADMM-NET is superior to the ADMM-based iterative algorithm in complexity. Moreover, the number of learning parameters within ADMM-NET is  $I_n(3(N_tL)^2 + N_tL + 3M^2 + M)$ .

The computation in the  $q$ th hidden layer of black-box NN can be formulated as  $\mathbf{y}_q = g(\mathbf{W}_q\mathbf{y}_{q-1} + \mathbf{b}_q)$ , where  $\mathbf{y}_q \in \mathbb{R}^{F_q \times 1}$  and  $\mathbf{y}_{q-1} \in \mathbb{R}^{F_{q-1} \times 1}$  denote the output vectors of  $q$ th and  $(q-1)$ th layers,  $g(\cdot)$  denotes the non-linear activation function and  $F_q$  stands for the dimension of the  $q$ th hidden layer.  $\mathbf{W}_q \in \mathbb{R}^{F_q \times F_{q-1}}$  and  $\mathbf{b}_q$  refer to the weight matrix and offset vector in the  $q$ th hidden layer. Consequently, the computational complexity of black-box NN can be given by  $\mathcal{O}(\sum_{q=2}^Q F_{q-1}F_q + F_Q(2N_tL + 2M))$ , where  $Q$  denotes the number of hidden layers. Besides, there are  $\sum_{q=2}^Q F_{q-1}F_q + \sum_{q=2}^Q F_{q-1}$  learnable parameters in the black-box NN.

### D. Comparison Between ADMM-NET and Black-Box NN

In this subsection, we comprehensively compare the proposed ADMM-NET and black-box NN as below.



- Via unfolding the proposed ADMM-based iterative algorithm, each layer of ADMM-NET can be regarded as one iteration. However, the architecture of black-box NN lacks sufficient interpretability because the physical meaning of each operation is not clear.
- In order to fit the complicated non-linear mapping, the black-box NN contains a number of learnable parameters, requiring enormous training samples and time to fine tune. However, the ADMM-NET introduces much less learnable parameters to approximate the complicated operations, enjoying the advantages of higher training efficiency and lower training samples requirements.
- Black-box NN belongs to the general NN, which can be utilized to fit diverse non-linear mappings. In contrast, the ADMM-NET is tailored for (7) via unfolding the proposed ADMM-based iterative algorithm. Owing to the natural customization, ADMM-NET encounters the drawback of limited scope of applications, which is also the common drawback of all the deep unfolding NNs.
- Since the training labels are generated by the ADMM, it serves as an upper bound of the black-box NN with supervised learning. Moreover, unsupervised learning may be easily trapped in local optima due to the inherent training mechanism without training labels. Although the ADMM-NET is also trained in an unsupervised learning manner, it is expected to overcome this limitation by combining training data and domain knowledge, which is also verified by the simulation results in Section V.

## V. SIMULATION RESULTS AND DISCUSSION

In this section, simulation results are presented to verify the effectiveness of the proposed algorithms. If not specified, we set  $N_t = 10$ ,  $K = 2$ ,  $L = 10$ ,  $M = 10$ ,  $P = 5$  W,  $\mu = 1$ ,  $\epsilon = 10^{-3}$ ,  $f_0 = 1$  Hz,  $f_s = 30$  Hz,  $\theta_t = 0$ , and  $\nu = 0.1$ . Without loss of generality, we consider that all the channels are Gaussian and the desired communication symbols are binary phase shift keying (BPSK) symbols with half unit power. Similar to [15], we only consider the small-scale fading and scaling received signal is not needed. The black-box NN consists of 4 hidden layers, with 2048 neurons per hidden layer, i.e.,  $Q = 4$  and  $F_1 = \dots = F_4 = 2048$ . The SINR of users is defined as  $\text{SINR} = \frac{P}{\sigma^2}$  and the hyperparameters of ADMM-NET is presented in Table II. The simulation results, except in Fig. 4, Fig. 5, and Fig. 6, are averaged over 500 independent channel realizations and the percentage “%” of the DL-based algorithms can be obtained by dividing the values of these algorithms by that of the ADMM-based iterative algorithm. All the experiments are conducted on the two Intel CPUs Xeon Gold 6242R with 128GB RAM. The traditional iterative algorithm and black-box NN are taken into consideration for performance comparison, which are listed as below.

- ADMM: The proposed ADMM-based iterative algorithm.
- SL: The black-box NN with supervised learning. Moreover, the obtained sub-optimal solutions by the ADMM can be applied as the training labels.

TABLE II  
HYPERPARAMETERS OF ADMM-NET

Parameter	Value
LR ( $\eta$ )	$5 \times 10^{-5}$
LR decay	$1 \times 10^{-3}$
Number of episodes ( $\mathcal{E}$ )	30
Number of hidden layers ( $I_n$ )	4
Batch size	1
Number of samples ( $ \mathcal{D} $ )	200

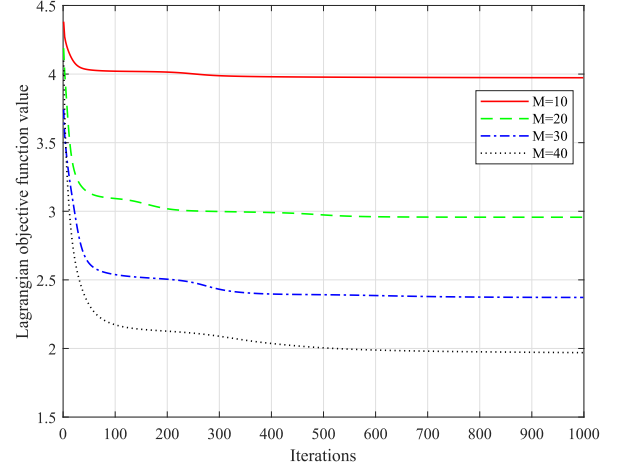


Fig. 4. Convergence of ADMM-based iterative algorithm versus  $M$ , with  $\rho = 0.5$ .

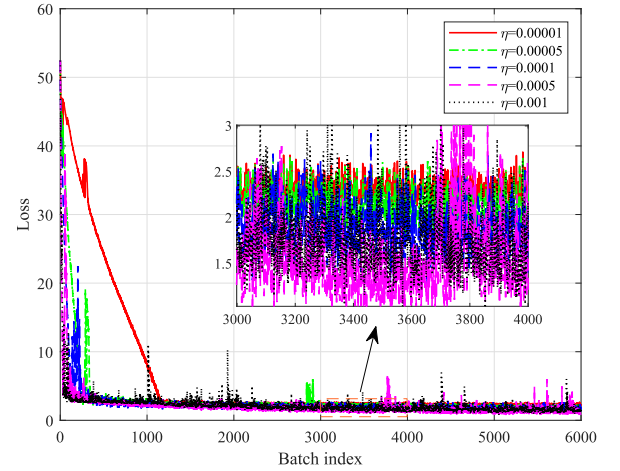


Fig. 5. Convergence of ADMM-NET versus the learning rate, with  $\rho = 0.5$ .

- USL: The black-box NN is trained in an unsupervised learning manner.

Both SL and USL are leveraged to learn the mapping from the problem statement to the corresponding solution in a full data-driven manner, which have been widely adopted in the literature.

Fig. 4 depicts the convergence of proposed ADMM-based iterative algorithm versus  $M$ , with  $\rho = 0.5$ . It can be seen that ADMM-based iterative algorithm converges within 1000 iterations, and the Lagrangian objective function value decreases with  $M$  owing to more degrees of freedom (DoF) at RIS. Nevertheless, larger  $M$  slows down the convergence

TABLE III  
PERFORMANCE OF ADMM-NET VERSUS  $I_n$ , WITH  $\rho = 0.5$

$I_n$	2	3	4	5	6	7	8
WSMEWD percentage	129.28%	106.77%	90.95%	97.54%	92.35%	<b>85.98%</b>	99.35%
Training time (minute)	25.20	39.17	52.00	65.65	79.67	93.32	107.27

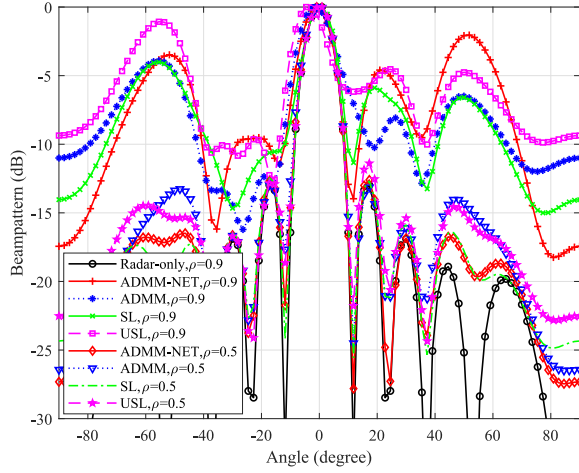


Fig. 6. Beampattern comparison among different algorithms.

TABLE IV  
PERFORMANCE COMPARISON VERSUS THE NUMBER OF TRAINING SAMPLES, WITH  $\rho = 0.5$

$ \mathcal{D} $	100	150	200	250	300
ADMM-NET	104.98%	100.03%	90.95%	89.03%	<b>83.12%</b>
SL	108.87%	106.98%	106.00%	105.50%	105.47%
USL	104.97%	103.26%	102.65%	101.22%	101.36%

speed because a larger solution space needs to explore. Consequently, there exists a trade-off between the performance and computational complexity.

Fig. 5 illustrates the convergence of ADMM-NET versus the learning rate, with  $\rho = 0.5$ . It can be seen that the convergence of ADMM-NET becomes faster with the learning rate. However, to guarantee the satisfactory convergence performance, the learning rate should be carefully chosen. Small learning rate alleviates the oscillation of the loss curve at the cost of slow convergence speed. In contrast, too large learning rate exacerbates the oscillation of the loss curve. Since the ADMM-NET with  $\eta = 0.00005$  can keep a good balance between convergence speed and stability, the learning rate of ADMM-NET is set as 0.00005 in the following.

Table III presents the performance of ADMM-NET versus  $I_n$ , with  $\rho = 0.5$ . We can observe that the training time increases with  $I_n$  owing to the increasing computation. When  $I_n$  is larger than 3, the ADMM-NET is superior to the ADMM owing to the stronger non-linear fitting capability. Although the ADMM-NET with  $I_n = 7$  achieves the best performance, it contains more learnable parameters, requiring more time to fine tune. To keep a balance between performance and training time, the number of hidden layers is set as  $I_n = 4$  in the following.

Table IV provides the performance comparison among different NNs versus the number of training samples, with

$\rho = 0.5$ . From Table IV, increasing training samples is beneficial to performance enhancement of each NN, and the ADMM-NET outperforms the ADMM when  $|\mathcal{D}|$  is larger than 150. Moreover, the SL is upper bounded by the ADMM because the training labels are generated by the ADMM-based iterative algorithm. Besides, increasing training samples brings limited performance enhancement of USL owing to the inherent training mechanism. Fortunately, the ADMM-NET can overcome these drawbacks of black-box NNs by combining the domain knowledge and training data, showcasing its superiority over both SL and USL.

Table V shows the CPU running time versus transmit antenna number at the ISAC-BS, with  $(\mathcal{E}, \rho) = (10, 0.5)$ . For fairness, the training time of the SL contains the time of obtaining the training labels by the ADMM-based iterative algorithm. We can see that the training time of all the three NNs increases with  $N_t$ , and the ADMM-NET requires more time to train than the benchmarks. Although there are less learnable parameters in the ADMM-NET, it consists of more complicated computing than the black-box counterparts per layer. In the inference stage, the ADMM-NET is superior to the ADMM-based iterative algorithm especially when  $N_t$  is large. Therefore, the ADMM-NET is a low-complexity alternative to the ADMM-based iterative algorithm. Nevertheless, both the SL and USL outperform the ADMM-NET in terms of the inference time due to the much simpler network architecture and operations. Owing to the same network architecture, the inference time of SL and USL is almost the same.

Fig. 6 presents the beampattern comparison among different algorithms. Moreover, the beampattern corresponding to the reference radar waveform is denoted as “Radar-only”. For each algorithm, the similarity between the obtained beampattern of each algorithm and “Radar-only” decreases with  $\rho$  because more DoF is leveraged to minimize the MUI. Moreover, for both  $\rho = 0.5$  and  $\rho = 0.9$ , the obtained beampattern of the ADMM-NET is more closer to “Radar-only” than those of other algorithms.

Fig. 7 illustrates the bit error ratio (BER) versus signal-to-noise ratio (SNR) for the proposed algorithm and benchmarks. From the results, the BER of each algorithm decreases as  $\rho$  increases because more DoF is leveraged to reduce the MUI. Therefore, the received signal is closer to the desired signal, facilitating the signal decoding. Since higher SNR is beneficial to decoding the received signal, BER decreases with SNR for all the algorithms. Although the ADMM is superior to both SL and USL, it is inferior to the ADMM-NET and the performance gap increases with SNR, verifying the effectiveness of the ADMM-NET.

In Fig. 8, we investigate the performance trade-off between the MUI energy and waveform discrepancy for the proposed algorithm and benchmarks. From Fig. 8, we observe that the MUI energy decreases with waveform discrepancy for all the

TABLE V  
CPU RUNNING TIME VERSUS THE NUMBER OF TRANSMIT ANTENNAS AT THE ISAC-BS, WITH  $(\mathcal{E}, \rho) = (10, 0.5)$

$N_t$	CPU training time (minute)			CPU testing time (second)			
	ADMM-NET	SL	USL	ADMM	ADMM-NET	SL	USL
5	18.1833	1.3333	1.0000	35.3867	14.5340	0.0117	0.0138
10	19.1667	3.4500	1.2167	133.5531	17.3970	0.0115	0.0108
15	27.1500	4.6000	1.2333	1436.4096	39.5808	0.0127	0.0115
20	28.6667	7.4000	1.2500	1842.4473	37.5796	0.0123	0.0124
25	29.4833	8.0833	1.3000	4033.9145	33.1324	0.0130	0.0152

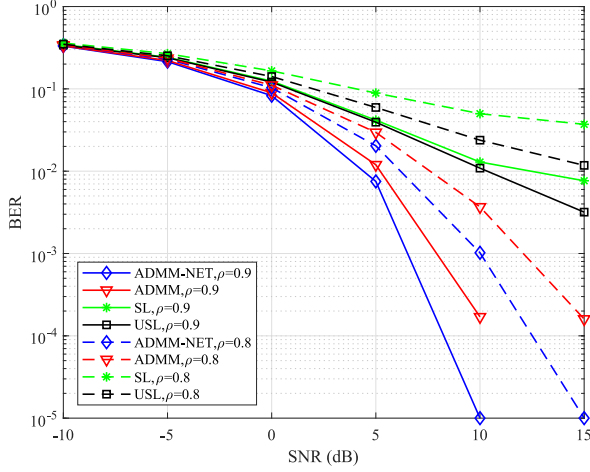


Fig. 7. BER versus SNR for the proposed algorithm and benchmarks.

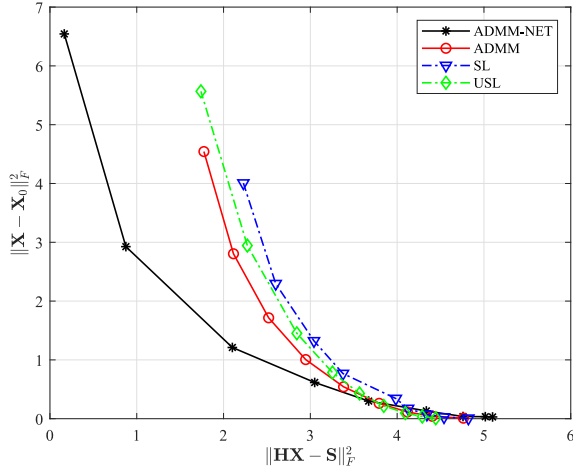


Fig. 8. Performance trade-off between the MUI energy and waveform discrepancy for the proposed algorithm and benchmarks.

algorithms owing to the limited spatial DoF and resource. Moreover, the ADMM-NET achieves the best performance trade-off among all the algorithms, and the ADMM is superior to both USL and SL. Consequently, the superiority of ADMM-NET is verified.

In Fig. 9, we study the average achievable rate versus the number of elements at RIS for the proposed algorithm and benchmarks, with  $(\rho, \text{SNR}) = (0.9, 10 \text{ dB})$ . From Fig. 9, for each algorithm, the achievable rate increases with  $M$  owing to the increased DoF and passive beamforming gain at RIS. Moreover, the USL is superior to the ADMM because it achieves smaller MUI energy than that of the ADMM

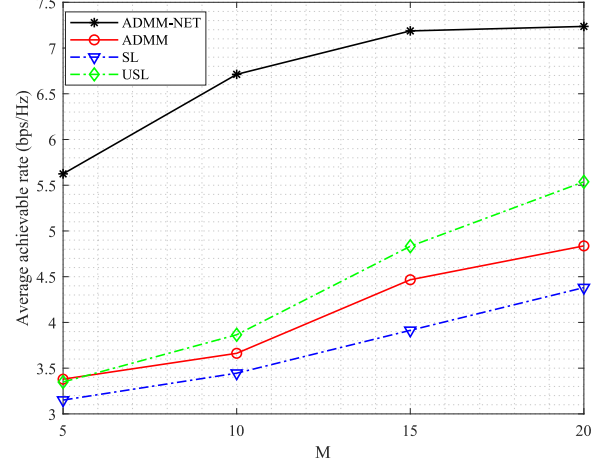


Fig. 9. Average Achievable rate versus the number of elements at RIS for the proposed algorithm and benchmarks, with  $(\rho, \text{SNR}) = (0.9, 10 \text{ dB})$ .

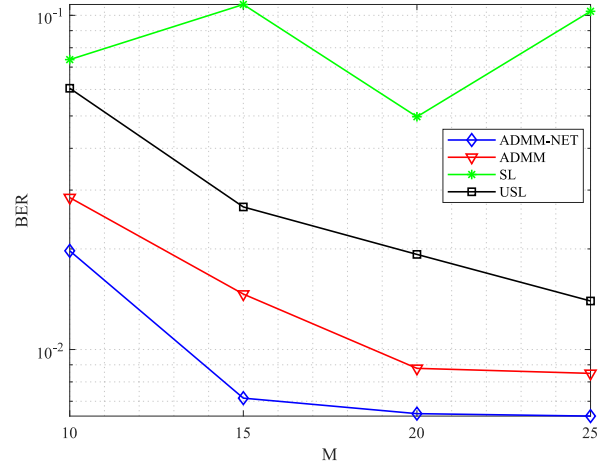


Fig. 10. BER versus the number of elements at RIS for the proposed algorithm and benchmarks, with  $(\rho, \text{SNR}) = (0.8, 5 \text{ dB})$ .

at the cost of larger waveform discrepancy, which can be concluded from Fig. 8. Besides, the ADMM-NET achieves the highest average achievable rate among all the algorithms, which verifies the effectiveness of the ADMM-NET.

Fig. 10 illustrates the BER versus the number of elements at RIS for the proposed algorithm and benchmarks, with  $(\rho, \text{SNR}) = (0.8, 5 \text{ dB})$ . It can be seen that the BER of all the algorithms except SL decreases with  $M$  owing to the increased DoF at RIS. In addition, the ADMM-NET is superior to the benchmarks, illustrating the effectiveness of the proposed ADMM-NET.

## VI. CONCLUSION

In this paper, we have proposed a low-complexity DF waveform design scheme for RIS-aided ISAC network based on deep unfolding learning. Specifically, the weighted sum of MUI energy and waveform discrepancy is minimized subject to the transmit power and constant modulus constraints by joint transmit waveform and phase shifts design. We first develop an ADMM-based iterative algorithm to deal with the non-convex problem. In particular, the original problem is divided into four subproblems, whose closed-form solutions are driven. Then, we propose a model-driven NN, named ADMM-NET, via unfolding the proposed ADMM-based iterative algorithm into a layer-wise architecture to further reduce the complexity and facilitate the online implementation. Moreover, the high-complexity matrix inversion is approximated by matrix multiplication with lower complexity. Simulation results demonstrate that the proposed ADMM-NET outperforms the ADMM-based iterative algorithm in both complexity and performance. Moreover, compared with the black-box counterparts, the ADMM-NET showcases the advantages of less learnable parameters, stronger interpretability and generalization capability.

## REFERENCES

- [1] J. Zhang, M. Liu, J. Tang, N. Zhao, N. Dusit, and X. Wang, "Joint waveform and passive beamforming design for IRS-aided ISAC via deep unfolding," in *Proc. IEEE WCSP*, 2024, pp. 1–6.
- [2] F. Liu, C. Masouros, A. P. Petropulu, H. Griffiths, and L. Hanzo, "Joint radar and communication design: Applications, state-of-the-art, and the road ahead," *IEEE Trans. Commun.*, vol. 68, no. 6, pp. 3834–3862, Jun. 2020.
- [3] M. Liu et al., "Performance analysis and power allocation for cooperative ISAC networks," *IEEE Internet Things J.*, vol. 10, no. 7, pp. 6336–6351, Apr. 2023.
- [4] W. Mao, Y. Lu, C.-Y. Chi, B. Ai, Z. Zhong, and Z. Ding, "Communication-sensing region for cell-free massive MIMO ISAC systems," *IEEE Trans. Wireless Commun.*, early access, Apr. 30, 2024, doi: [10.1109/TWC.2024.3392330](https://doi.org/10.1109/TWC.2024.3392330).
- [5] Y. Zhong et al., "Empowering the V2X network by integrated sensing and communications: Background, design, advances, and opportunities," *IEEE Netw.*, vol. 36, no. 4, pp. 54–60, Jul./Aug. 2022.
- [6] M. B. Mollah, H. Wang, M. A. Karim, and H. Fang, "mmWave enabled connected autonomous vehicles: A use case with V2V cooperative perception," *IEEE Netw.*, early access, Oct. 13, 2023, doi: [10.1109/MNET.2023.3321520](https://doi.org/10.1109/MNET.2023.3321520).
- [7] Y. Cui, F. Liu, X. Jing, and J. Mu, "Integrating sensing and communications for ubiquitous IoT: Applications, trends, and challenges," *IEEE Netw.*, vol. 35, no. 5, pp. 158–167, Sep./Oct. 2021.
- [8] M. B. Mollah, M. A. K. Azad, and Y. Zhang, "Secure targeted message dissemination in IoT using blockchain enabled edge computing," *IEEE Trans. Consum. Electron.*, to be published.
- [9] Q. Wu et al., "A comprehensive overview on 5G-and-beyond networks with UAVs: From communications to sensing and intelligence," *IEEE J. Sel. Areas Commun.*, vol. 39, no. 10, pp. 2912–2945, Oct. 2021.
- [10] J. Xu, D. Li, Z. Zhu, Z. Yang, N. Zhao, and D. Niyato, "Anti-jamming design for integrated sensing and communication via aerial IRS," *IEEE Trans. Commun.*, vol. 72, no. 8, pp. 4607–4619, Aug. 2024.
- [11] A. Hassanien, M. G. Amin, Y. D. Zhang, and F. Ahmad, "Dual-function radar-communications: Information embedding using sidelobe control and waveform diversity," *IEEE Trans. Signal Process.*, vol. 64, no. 8, pp. 2168–2181, Apr. 2016.
- [12] A. Hassanien, M. G. Amin, Y. D. Zhang, F. Ahmad, and B. Himed, "Non-coherent PSK-based dual-function radar-communication systems," in *Proc. IEEE RadarConf*, 2016, pp. 1–6.
- [13] D. Ma, N. Shlezinger, T. Huang, Y. Liu, and Y. C. Eldar, "FRaC: FMCW-based joint radar-communications system via index modulation," *IEEE J. Sel. Topics Signal Process.*, vol. 15, no. 6, pp. 1348–1364, Nov. 2021.
- [14] Z. Wei et al., "Waveform design for MIMO-OFDM integrated sensing and communication system: An information theoretical approach," *IEEE Trans. Commun.*, vol. 72, no. 1, pp. 496–509, Jan. 2024.
- [15] F. Liu, L. Zhou, C. Masouros, A. Li, W. Luo, and A. Petropulu, "Toward dual-functional radar-communication systems: Optimal waveform design," *IEEE Trans. Signal Process.*, vol. 66, no. 16, pp. 4264–4279, Aug. 2018.
- [16] J. Zhu, W. Li, K.-K. Wong, T. Jin, and K. An, "Waveform design of DFRC system for target detection in clutter environment," *IEEE Signal Process. Lett.*, vol. 30, pp. 1517–1521, Oct. 2023.
- [17] R. Liu, M. Li, Q. Liu, and A. L. Swindlehurst, "Dual-functional radar-communication waveform design: A symbol-level precoding approach," *IEEE J. Sel. Topics Signal Process.*, vol. 15, no. 6, pp. 1316–1331, Nov. 2021.
- [18] M. Shi, X. Li, J. Liu, and S. Lv, "Constant modulus waveform design for RIS-aided ISAC system," *IEEE Trans. Veh. Tech.*, vol. 73, no. 6, pp. 8648–8659, Jun. 2024.
- [19] K. Zhong, J. Hu, C. Pan, M. Deng, and J. Fang, "Joint waveform and beamforming design for RIS-aided ISAC systems," *IEEE Signal Process. Lett.*, vol. 30, pp. 165–169, Feb. 2023.
- [20] Y. Du, Y. Liu, K. Han, J. Jiang, W. Wang, and L. Chen, "Multi-user and multi-target dual-function radar-communication waveform design: Multi-fold performance tradeoffs," *IEEE Trans. Green Commun. Netw.*, vol. 7, no. 1, pp. 483–496, Mar. 2023.
- [21] Z. Yin et al., "DDSNet: Deep dual-branch networks for surface defect segmentation," *IEEE Trans. Instrum. Meas.*, vol. 73, pp. 1–16, Jul. 2024.
- [22] G. Han, J. Chen, L. Liu, Z. Wang, F. Zhang, and Y. Abudurexiti, "An interpretable CNN with wavelet group policy embedded for intelligent fault diagnosis," *IEEE Trans. Instrum. Meas.*, vol. 73, pp. 1–15, Feb. 2024.
- [23] X. Zhang et al., "Robust DNN-based recovery of wideband spectrum signals," *IEEE Wireless Commun. Lett.*, vol. 12, no. 10, pp. 1712–1715, Oct. 2023.
- [24] M. Zhang, S. Wu, J. Jiao, N. Zhang, and Q. Zhang, "Energy- and cost-efficient transmission strategy for UAV trajectory tracking control: A deep reinforcement learning approach," *IEEE Internet Things J.*, vol. 10, no. 10, pp. 8958–8970, May 2023.
- [25] Z. Zhu, C. Shen, H. Yu, Z. Wang, Z. Shen, and J. Du, "Deep learning for waveform level receiver design with natural redundancy," *IEEE Trans. Cogn. Commun. Netw.*, vol. 9, no. 2, pp. 317–331, Apr. 2023.
- [26] Y. Shi et al., "Machine learning for large-scale optimization in 6G wireless networks," *IEEE Commun. Surveys Tuts.*, vol. 25, no. 4, pp. 2088–2132, 4th Quart., 2023.
- [27] Y. Zhao, Z. Wang, Z. Wang, X. Chen, and Y. Zhou, "Learning to beamform for dual-functional MIMO radar-communication systems," in *Proc. IEEE ICC*, Rome, Italy, 2023, pp. 3572–3577.
- [28] X. Liu, H. Zhang, K. Long, A. Nallanathan, and V. C. M. Leung, "Distributed unsupervised learning for interference management in integrated sensing and communication systems," *IEEE Trans. Wireless Commun.*, vol. 22, no. 12, pp. 9301–9312, Dec. 2023.
- [29] Y. Li, Y. Lu, R. Zhang, B. Ai, and Z. Zhong, "Deep learning for energy efficient beamforming in MU-MISO networks: A GAT-based approach," *IEEE Wireless Commun. Lett.*, vol. 12, no. 7, pp. 1264–1268, Jul. 2023.
- [30] H. He, S. Jin, C.-K. Wen, F. Gao, G. Y. Li, and Z. Xu, "Model-driven deep learning for physical layer communications," *IEEE Wireless Commun.*, vol. 26, no. 5, pp. 77–83, Oct. 2019.
- [31] V. Monga, Y. Li, and Y. C. Eldar, "Algorithm unrolling: Interpretable, efficient deep learning for signal and image processing," *IEEE Signal Process. Mag.*, vol. 38, no. 2, pp. 18–44, Mar. 2021.
- [32] J. Gao, C. Zhong, G. Y. Li, and Z. Zhang, "Deep learning-based channel estimation for massive MIMO with hybrid transceivers," *IEEE Trans. Wireless Commun.*, vol. 21, no. 7, pp. 5162–5174, Jul. 2022.
- [33] Q. Hu, Y. Cai, Q. Shi, K. Xu, G. Yu, and Z. Ding, "Iterative algorithm induced deep-unfolding neural networks: Precoding design for multiuser MIMO systems," *IEEE Trans. Wireless Commun.*, vol. 20, no. 2, pp. 1394–1410, Feb. 2021.
- [34] I. N. Tiba, Q. Zhang, J. Jiang, and Y. Wang, "A low-complexity Admm-based massive MIMO detectors via deep neural networks," in *Proc. IEEE ICASSP*, Toronto, ON, Canada, 2021, pp. 4930–4934.
- [35] N. T. Nguyen et al., "Deep unfolding hybrid beamforming designs for THz massive MIMO systems," *IEEE Trans. Signal Process.*, vol. 71, pp. 3788–3804, Oct. 2023.
- [36] N. T. Nguyen, L. V. Nguyen, N. Shlezinger, Y. C. Eldar, A. L. Swindlehurst, and M. Juntti, "Joint communications and sensing hybrid beamforming design via deep unfolding," 2023, [arXiv:2307.04376](https://arxiv.org/abs/2307.04376).



- [37] P. Krishnananthalingam, N. T. Nguyen, and M. Juntti, "Deep unfolding enabled constant modulus waveform design for joint communications and sensing," 2023, *arXiv:2306.14702*.
- [38] S. He, S. Xiong, Z. An, W. Zhang, Y. Huang, and Y. Zhang, "An unsupervised deep unrolling framework for constrained optimization problems in wireless networks," *IEEE Trans. Wireless Commun.*, vol. 21, no. 10, pp. 8552–8564, Oct. 2022.
- [39] J. Xu, C. Kang, J. Xue, and Y. Zhang, "A fast deep unfolding learning framework for robust MU-MIMO downlink precoding," *IEEE Trans. Cogn. Commun. Netw.*, vol. 9, no. 2, pp. 359–372, Apr. 2023.
- [40] R. Liu, M. Li, Y. Liu, Q. Wu, and Q. Liu, "Joint transmit waveform and passive beamforming design for RIS-aided DFRC systems," *IEEE J. Sel. Topics Signal Process.*, vol. 16, no. 5, pp. 995–1010, Aug. 2022.
- [41] R. A. Horn and C. R. Johnson, *Matrix Analysis*. Cambridge, U.K.: Cambridge Univ., 2012.
- [42] S. Boyd, N. Parikh, E. Chu, B. Peleato, and J. Eckstein, "Distributed optimization and statistical learning via the alternating direction method of multipliers," *Found. Trends Mach. Learn.*, vol. 3, no. 1, pp. 1–122, 2010.
- [43] Y. Liu, Q. Hu, Y. Cai, G. Yu, and G. Y. Li, "Deep-unfolding beamforming for intelligent reflecting surface assisted full-duplex systems," *IEEE Trans. Wireless Commun.*, vol. 21, no. 7, pp. 4784–4800, Jul. 2022.



**Jifa Zhang** received the M.S. degree from Beihang University, China, in 2023. He is currently pursuing the Ph.D. degree with the School of Information and Communication Engineering, Dalian University of Technology, China. His current research interests include unmanned aerial vehicle communications, deep learning, optimization theory, and intelligent reflection surface.



Engineering, Virginia Tech, Blacksburg, VA, USA. His research interests include communication signal processing, statistical signal processing and artificial intelligence.



**Jie Tang** (Senior Member, IEEE) received the B.Eng. degree from the South China University of Technology, China, the M.Sc. degree from the University of Bristol, U.K., and the Ph.D. degree from Loughborough University, U.K.

From 2013 to 2015, he was a Research Associate with the School of Electrical and Electronic Engineering, University of Manchester, U.K. He is currently a Professor with the School of Electronic and Information Engineering, South China University of Technology. His current research interests include SWIPT, UAV communications, NOMA, and reconfigurable intelligent surface. He is a co-recipient of the ICNC 2018, CSPS 2018, WCSP 2019, and 6GN 2020 Best Paper Awards. He is currently serving as an Editor for IEEE WIRELESS COMMUNICATIONS LETTERS, IEEE SYSTEMS JOURNAL, and IEEE ACCESS. He is the Guest Editor for two special issues in IEEE TRANSACTIONS ON GREEN COMMUNICATIONS AND NETWORKING, and one special issue in IEEE OPEN JOURNAL OF THE COMMUNICATIONS SOCIETY. He also served as the Track Co-Chair of IEEE VTC-Spring 2018, the Symposium Co-Chair of IEEE/CIC ICC 2020 and IEEE ComComAp 2019, the TPC Co-Chair of EAI GreeNets 2019, and the Workshop Co-Chair of IEEE ICC/CIC 2019.



WIRELESS COMMUNICATIONS LETTERS.

**Nan Zhao** (Senior Member, IEEE) received the Ph.D. degree in information and communication engineering from the Harbin Institute of Technology, Harbin, China, in 2011. He is currently a Professor with the Dalian University of Technology, China. He won the Best Paper Awards in IEEE VTC 2017 Spring, ICNC 2018, WCSP 2018 and WCSP 2019. He also received the IEEE Communications Society Asia Pacific Board Outstanding Young Researcher Award in 2018. He is serving on the editorial boards of IEEE WIRELESS COMMUNICATIONS and IEEE



**Dusit Niyato** (Fellow, IEEE) received the B.Eng. degree from the King Mongkuts Institute of Technology Ladkrabang, Thailand, and the Ph.D. degree in electrical and computer engineering from the University of Manitoba, Canada. He is a Professor with the College of Computing and Data Science, Nanyang Technological University, Singapore. His research interests are in the areas of mobile generative AI, edge intelligence, decentralized machine learning, and incentive mechanism design.



**Xianbin Wang** (Fellow, IEEE) received the Ph.D. degree in electrical and computer engineering from the National University of Singapore in 2001.

He is a Professor and a Tier-1 Canada Research Chair of 5G and Wireless IoT Communications with Western University, Canada. Prior to joining Western University, he was with the Communications Research Centre Canada as a Research Scientist/Senior Research Scientist from 2002 to 2007. From 2001 to 2002, he was a System Designer with STMicroelectronics. He has over 600 highly cited journals and conference papers, in addition to over 30 granted and pending patents and several standard contributions. His current research interests include 5G/6G technologies, Internet of Things, machine learning, communications security, and intelligent communications.

Dr. Wang has received many prestigious awards and recognitions, including the IEEE Canada R. A. Fessenden Award, the Canada Research Chair, the Engineering Research Excellence Award at Western University, the Canadian Federal Government Public Service Award, the Ontario Early Researcher Award, and nine Best Paper Awards. He was involved in many IEEE conferences, including GLOBECOM, ICC, VTC, PIMRC, WCNC, CCECE, and CWIT, in different roles, such as the general chair, the TPC chair, the symposium chair, the tutorial instructor, the track chair, the session chair, and a keynote speaker. He serves/has served as the Editor-in-Chief, the Associate Editor-in-Chief, and an editor/associate editor for over ten journals. He was the Chair of the IEEE ComSoc Signal Processing and Computing for Communications Technical Committee and is currently serving as the Central Area Chair of IEEE Canada. He is a Fellow of the Canadian Academy of Engineering and a Fellow of the Engineering Institute of Canada.